Journal of Applied Fluid Mechanics, Vol. 17, No. 4, pp. 828-843, 2024.
Available online at www.jafmonline.net, ISSN 1735-3572, EISSN 1735-3645.
https://doi.org/10.47176/jafm.17.4.2235

Effect of Semi-elliptical Outer Blade-surface on the Savonius Hydrokinetic Turbine Performance: A Numerical Investigation

G. V. Babu and D. K. Patel†

School of Mechanical Engineering, Vellore Institute of Technology, Vellore – 632014, India

†*Corresponding Author Email: devendrakumar.patel@vit.ac.in*

ABSTRACT

The Savonius hydrokinetic turbine (SHT) is widely used for generating electricity from running water. However, most optimization work has been carried out on conventional blades with similar concave and convex profiles. This study aims to enhance SHT performance by modifying the rotor blades' outer surface radius (0.079, 0.087 and 0.095 m) to create a semi-elliptical shape, thus reducing opposing forces. The tip speed ratio (TSR) varies from 0.5 to 1.3 with an interval of 0.1. A constant channel velocity of 0.8 m/s at Re = 2.25×10^5 is considered for the analysis. The flow field has been numerically investigated using the SST k - ω model. This study comprises the angular variation in the coefficients of power (C_p) and torque (C_m), performance curves of the rotor, and pressure distribution on the blade surface at different angular positions. It is observed that the rotor with a radius of 0.095 m has a maximum C_p value of 0.142, which is 7.57% and 18.33% higher than the C_p values of rotors with radii of 0.079 m and 0.087 m, respectively. The maximum power output of the rotor with a radius of 0.095 m is 2.32 W, whereas the power outputs of the rotors with radii of 0.087 m and 0.079 m are 2.16 W and 1.96 W, respectively. An increase in the instantaneous values of C_m between rotation angles 0° to 115° is observed, during which the returning blades mainly interact with the incoming stream. The pressure decreases as the radius of the semi-elliptical outer surface increases at rotor positions ranging from 0° to 225°, but it increases at rotor positions ranging from 270° to 315°.

Article History

Received August 19, 2023
Revised November 19, 2023
Accepted November 23, 2023
Available online January 30, 2024

Keywords:

SHT
Power and torque coefficients
SST k - ω model
Flow characteristics
Computational fluid dynamics
OpenFOAM

1. INTRODUCTION

In remote locations, generating electricity from running water is an eco-friendly and cost-effective solution. A hydrokinetic turbine is generally suitable for these purposes due to its simple design and easy installation (Boccaletti et al., 2008). If the flowing medium is not considered, then it can be said that a hydrokinetic turbine works on the principles of wind turbine. Since water is denser than air, a hydrokinetic turbine can generate more power than a comparable wind turbine (Khan et al., 2009). Hydrokinetic turbines are classified into two types based on installation: axial-flow rotors and cross-flow rotors. Vertical-axis turbines, which are a type of cross-flow rotor, are more suitable for narrow channels or low-flow rivers. Savonius (Salleh et al., 2019) and Darrieus (Wong et al., 2017) are commonly referred to as vertical axis hydrokinetic turbines which are often used to be installed in channels. The Savonius is considered a superior because of its higher starting torque output than Darrieus (Kamal & Saini, 2022). The Savonius Hydrokinetic Turbine (SHT) is simple in design and produces low noise. It accepts fluid flow in any direction and has excellent starting characteristics at low speeds.

A number of investigations have been carried out over the past few decades through experimental and analytical studies to improve the performance of SHT. However, traditional Savonius turbines have lower efficiency than most lift-type wind turbines, such as horizontal axis wind turbines and Darrieus wind turbines. The performance of Savonius turbines are influenced by the number of blades, blade shape, overlap ratio, gap ratio, stages, guide plates, end plates and other accessories. In the aspect of blade shape, Wahyudi et al. (2013) designed three new types of Tandem Blade Savonius (TBS) rotors that improve the drag force generation by enlarging the swept area. The first type has an overlapping blade arrangement, the second has a symmetrical blade arrangement, and the third

NOMENCLATURE

A	projected area of the rotor
a_1	a constant
arg_1	function defined by the Eq. (16)
arg_2	function defined by the Eq. (20)
$CD_{k\omega}$	function related to the cross-diffusion term by Eq. (17)
C_m	coefficient of torque
C_p	coefficient of power
D	rotor diameter
F_1 *and* F_2	blending functions
k	turbulent kinetic energy
N	rotor speed
p	pressure
$P_{available}$	power available in flow field
P_{rotor}	rotors power output
R	rotor radius
r	blade inner surface radius
r_A, r_B and r_C	blade outer surface semi-elliptical major radius
R_d	radial distance from the rotor center
T	rotor torque output
U	velocity of the upstream flow
y^+	y-plus value
Re	Reynolds number

Greek Symbols

β^*	SST k - ω turbulence model constant
β_1, γ_1 σ_{k1}, and $\sigma_{\omega 1}$	standard k - ω turbulence model constant
β_2, γ_2 σ_{k2}, and $\sigma_{\omega 2}$	standard k - ϵ turbulence model constant
λ_2	lambda2
μ	dynamic viscosity
μ_t	eddy or turbulent viscosity
ν	kinematic viscosity of water
ν_t	turbulent kinematic viscosity
ω	turbulent specific dissipation rate
ω_z	vortex component in z-direction
ϕ	SST k - ω turbulence model constant
ϕ_1	k - ω turbulence model constant
ϕ_2	k - ϵ turbulence model constant
ρ	water density
τ_{ij}	stress tensor
Ω	rotational velocity

Abbreviations

k - ϵ	turbulence kinetic energy - turbulent dissipation rate
k - ω	turbulence kinetic energy - turbulent specific dissipation rate
AMI	Arbitrary Mesh Interface
AR	Aspect Ratio
RANS	Reynolds Averaged Navier-Stokes
SHT	Savonius Hydrokinetic Turbine
SST k - ω	Shear stress transport - Turbulence kinetic energy - turbulent specific dissipation rate
TSR	Tip Speed Ratio

has a converging type of blade arrangement. Among the three designs, the converging type TBS showed best efficiency and provided maximum pressure difference between upstream and downstream. Tartuferi et al. (2015) developed two new rotor designs (*SR*3345 and *SR*5050) to improve the performance of the conventional Savonius wind turbine by implementing a significant increase in the mean camber line of the base airfoil shape. It was noticed that both of these rotor designs take advantage of low-pressure regions behind the advancing blade, which can make a favorable contribution to rotor rotation and thus enhances the power output. The profiles of concave and convex surfaces were modified to better the performance of the Savonius wind rotor by Tian et al. (2017). It was found that the modified rotor performed 4.41% better than the conventional Savonius wind turbine. The modified rotor had stronger recovery flow and tip vortices. Kacprzak et al. (2013) analyzed three types of Savonius rotors: classical, Bach-type and elliptical. Based on the torque and power characteristics, reported that the Bach-type rotor performs well in the range of TSR from 0.5 to 1.1, and the elliptical rotor performs better in the TSR range of 0.2 to 0.4. Tian et al. (2015) developed a unique rotor shape based on Myring Equation. The study was conducted with a constant velocity of 7 m/s while altering the TSR range from 0.4 to 1.2. It was concluded that a 10.98% improvement was achieved with the unique rotor compared to the conventional rotor. Kumar and Saini (2017) studied a modified SHT having twisted blades by altering the upstream velocities (0.5 to 2 m/s). It was stated that the performance of SHT improves with increase in upstream velocity. In addition, the optimum geometric parameter with blade arc angle of 150° and blade shape factor is found to be 0.6. In the other accessories aspect, Kailash et al. (2012) added a series of deflector plates to divert the upstream to the concave side of the forward blade and at the same time prevents the flow of the upstream to the convex side of the returning blade. As a result, at TSR 1.08, the value of Cp increases to 0.35. Talukdar et al. (2018) analyzed the flow characteristics of semicircular-shaped (two and three bladed) and elliptical-shaped SHT at a uniform upstream velocity of 0.8 m/s. The highest values of C_p for semicircular- shaped SHT 0.84 and 0.67 were obtained at TSR values of 0.28 and 0.17 respectively. It is observed that semicircular-shaped SHT have better flow characteristics than elliptical-shaped SHT. Mohamed et al. (2010) conducted a numerical study on a three-blade Savonius turbine by varying the blade design, gap ratio, and overlap ratio. In addition, they have used end plate, number of blades, guide plates, and specific attachments in order to improve the performance of three-blade SHT. In this optimization procedure, it was

found the conventional three-blade SHT, especially at TSR = 0.7, leading to a relative increase in power output coefficient by 57%. Mahmoud et al. (2012) performed an experimental study on Savonius rotors (two, three and four bladed) and different aspect ratios (0.5, 1, 2, 4 and 5). The two-blade rotor was found more efficient among the other configurations and stated that C_p increases with increase in aspect ratio. Basumatary and Biswas (2016) studied the performance of a two bladed SHT at different upstream velocities (1.5, 1.1, 0.9, 0.65 and 0.3m/s) using a deflector, and optimized the position of the deflector through power curves. At a free stream velocity of 0.9 m/s, a maximum C_p value 0.54 was observed at TSR 0.578. The experimental analysis performed by Patel et al. (2016) reported that the optimal performance of SHT was achieved at overlap ratio = 0.11 and aspect ratio (AR) 0.60. Whereas it a stable performance of SHT for lower AR ≤ 1.8 was observed. Yuwono et al. (2018) analyzed the influence of a single plate's width placed in front of the returning blade on the performance of SHT through an experimental and analytical studies. It was found that the performance of the rotor increases with wider plate at higher Reynolds numbers. Setiawan et al. (2019a,b) reported that the C_p of SHT can be increased by 17.3% over conventional SHT at TSR of 0.9 by keeping a circular cylinder in front of the advancing blade at certain angles. Anthony and Roy (2020) conducted a two dimensional (2D) numerical analysis on SHT by modifying the blade profile on different Reynolds number varying from 0.71×10^5 to 1.88×10^5 and obtained higher values of C_p compared to conventional SHT. An experimental analysis by Salleh et al. (2020) considering a deflector in front of two and three bladed rotors was conducted in a closed wind tunnel with a wind speed of 10 m/s. It has been observed that the performance of the rotors is greatly improved when the deflector is used at an angle of 60°. Alizadeh et al. (2020) performed three-dimensional numerical analysis on the SHT by placing a circular barrier in front of the returning blade. The analysis was performed by dividing the circular barrier into nine sectors, where a uniform free stream velocity of 7 m/s was considered. Compared to the conventional rotor, the C_m of the circular barrier rotor was found to increase by 19% at TSR 0.8. Chen et al. (2023) developed an efficient deflector system for a bidirectional cluster using a genetic algorithm and the kriging method, which produced a 34.5% improvement in Cp over the cluster without deflectors. The study concluded that deflectors increased the magnitude and strength of the low pressure at the advancing blade while decreasing the pressure area at the returning blade. Abdelghafar et al. (2023) proposed a bionic blade shape to enhance the efficiency of a conventional Savonius wind rotor. These blade shapes are inspired by sandeels (fish) and optimized to maximize performance. It was reported to exhibit a significant improvement in rotor efficiency of 9.21% at a TSR of 0.8 when compared to a rotor design with semi-circular blades. The pressure vibration and internal flow field of axial-flow pumps were quantitatively and qualitatively analyzed by Al-Obaidi (2018, 2019, 2023a,b); Al-Obaidi et al. (2023); Al-Obaidi et al. (2023a,b); Al-Obaidi and Qubian (2022) using experimental and CFD numerical methods. The study examined the influence of varying diffusers and impeller angles on the design and performance of flow fields in axial flow pumps during transient conditions. The k - ϵ turbulence model and sliding grid method are used in the investigations. The numerical results offer theoretical guidance for future research and the design of axial flow rotors.

The literature review shows that an extensive analysis has been performed by researchers to optimize the Savonius Hydrokinetic Turbine (SHT). However, most of the optimization work has been carried out considering the 'thin' blades, which have similar concave and convex profiles on both sides. Some authors worked on the different thicknesses of the blades by modifying the concave side. During the forward motion of the blade, the upstream primarily affects the concave surface of the blade, while during the return motion, the convex surface plays an important role. An optimized convex surface design can reduce the opposing torque, ultimately improving the rotor's performance. The present numerical analysis deals with optimizing the convex surface on the advancing and returning blades by using semi-elliptical outer surfaces. Three cases have been considered by modifying the semi-elliptical outer surfaces. For the analysis, a constant channel velocity of 0.8 m/s at Re = 2.25×10^5 has been considered, and the tip speed ratio (TSR) ranges from 0.5 to 1.3 with an interval of 0.1. The incompressible flow field has been solved using the SST k - ω model in OpenFOAM (2017). An attempt has been made to understand the interaction of rotor blades with fluid flow by using various contour plots at different angular positions of the rotor. The flow patterns close to the rotors are described using the streamlines and velocity vectors over the pressure contours, while shearing-swirling zones are identified using the λ_2 criterion. The angular variations in the instantaneous coefficient of torque (C_m) of different rotors are compared using the polar plot. The pressure distribution on the concave and convex surfaces of the rotor blades has been studied at different rotation angles. Some significant conclusions have been drawn based on the performance of different cases.

2. COMPUTATIONAL PROCEDURE

2.1 Rotor Design and Computational Domain

The schematic diagram of a rotor blade is illustrated in Fig. 1. In the present study, rotor blades are modified by changing the major radius (r_A, r_B and r_C) of the semi-elliptical outer surface to reduce the opposing forces on the returning blade. Whereas the inner surface radius (r) kept constant.

The dimensions of the different geometrical parameter considered in the present design of the rotor blades are exhibited in Table 1. In the present study the rotor is operating in a water channel and assumed to be completely submerged in the water. The rotor blades are identical throughout the axis of the rotor which allows two-dimensional (2D) of the present problem. When a propeller aspect ratio (AR) is equal to or greater than one, 2D analysis can accurately predict the flow dynamics (Anthony & Roy, 2020). Figure 2 depicts a schematic

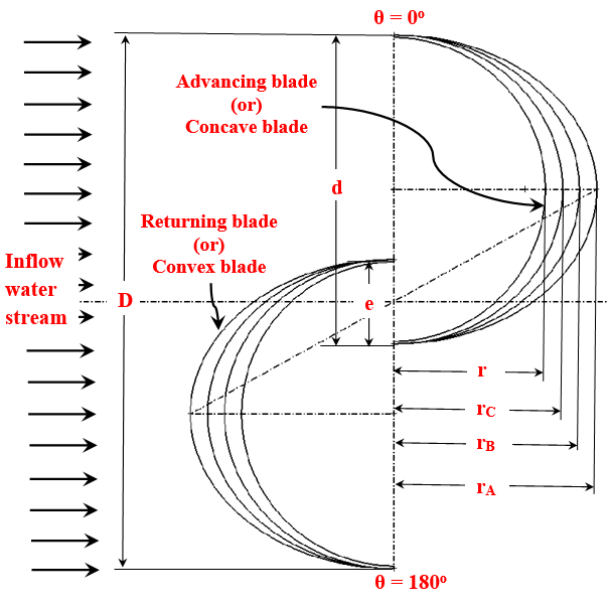

Fig. 1 Schematic diagram of a rotor blade

Table 1 Geometrical parameters of SHT

Parameters	Values (m)
Rotor diameter (D)	0.25
Blade diameter (d)	0.144
Blade inner surface radius (r)	0.072
Case-*A* blade outer surface radius (r_A)	0.095
Case-*B* blade outer surface radius (r_B)	0.087
Case-*C* blade outer surface radius (r_C)	0.079
Overlap distance (e)	0.037

diagram of the 2D computational domain. A computational domain of size 12D × 6D is considered based on the previous studies. The rotor is placed 4D away from the inlet and has an equal distance from the left and right walls. The computational domain has been subdivided into stationary and rotating domains, which is separated by Arbitrary Mesh Interface (AMI) of a diameter 1.5D as depicted in Fig. 2.

2.2 Performance Variables

The conceptual background for hydrokinetic turbines is taken from traditional wind turbine research. The coefficient of torque (C_m), coefficient of power (C_p) and the tip-speed ratio (TSR) are commonly used to describe the performance of turbines. These performance variables are defined as follows: (Zhao et al., 2009; Talukdar et al., 2018; Salleh et al., 2019)

$$C_p = \frac{P_{rotor}}{P_{available}} \tag{1}$$

$$P_{available} = \frac{1}{2}\rho A U^3 \tag{2}$$

$$P_{rotor} = \frac{2\pi N T}{60} \tag{3}$$

$$C_m = \frac{T}{\frac{1}{2}\rho A U^2 R} = \frac{C_p}{TSR} \tag{4}$$

$$TSR = \frac{\Omega R}{U} \tag{5}$$

where, ρ is water density (kg/ m^3) , P_{rotor} is rotors power output (W), $P_{available}$ is power available in flow field (W), U is the velocity of the upstream flow (m/s), A is the projected area of the rotor (m^2), T is rotor torque output (N-m), N is rotor speed (rpm), Ω is rotational velocity (rad/s), D is rotor diameter (m) and $R = D/2$ is rotor radius (m).

2.3 Mathematical Model

The transient, two-dimensional, incompressible turbulent flow field considered in the present study is solved numerically using the SST k - ω RANS approach. A variety of turbulence models have been introduced in the literature (Sarma et al., 2014; Talukdar et al., 2018; Setiawan et al., 2019a; Alizadeh et al., 2020), based on the Reynolds number as well as turbine geometry. The SST k - ω turbulence model is a combination of k - ω and k - ϵ

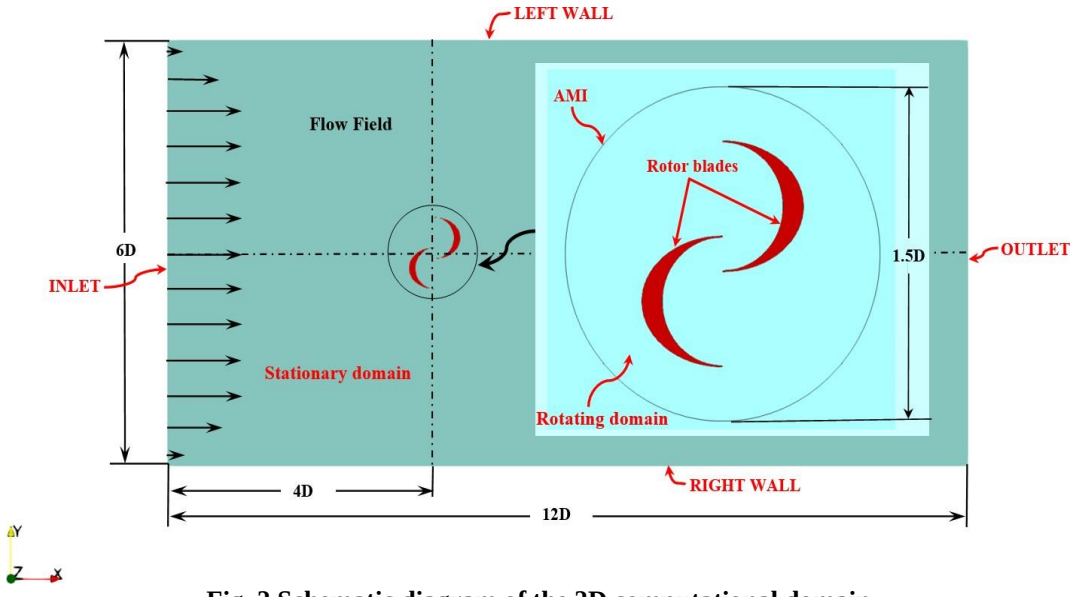

Fig. 2 Schematic diagram of the 2D computational domain

turbulence models so that the k - ω model is used in the viscous sub-layer where the high accuracy of the boundary layer is required and the k - ϵ model is used in the free shear flow outside the boundary layer. This SST k - ω turbulence model with two equations accurately predicts a wide range of flows, including rotational flow, flow over airfoils, low Reynolds number flow and flow with a negative pressure gradient (Menter, 1994; Roy & Ducoin, 2016; Basumatary et al., 2018).

The continuity and momentum equations used in RANS approach with Boussinesq approximation are presented in Eq. 6 and Eq. 7. (Menter, 1994; Roy & Ducoin, 2016)

$$\frac{\partial u_i}{\partial x_i} = 0 \tag{6}$$

$$\frac{\partial u_i}{\partial t} + \frac{\partial u_i u_j}{x_j} = -\frac{1}{\rho}\left[\frac{\left(\partial p + \partial \frac{2}{3}\rho k\right)}{\partial x_i}\right] + \frac{\partial}{\partial x_j}\left[\frac{1}{\rho}(\mu + \mu_t)\frac{\partial U_i}{\partial x_j}\right] \tag{7}$$

Original k - ω model (Wilcox k - ω model): (Menter, 1994; Roy & Ducoin, 2016)

$$\frac{D\rho k}{Dt} = \tau_{ij}\frac{\partial u_i}{\partial x_j} - \beta^*\rho\omega k + \frac{\partial}{\partial x_j}\left[(\mu + \sigma_{k_1}\mu_t)\frac{\partial k}{\partial x_j}\right] \tag{8}$$

$$\frac{D\rho\omega}{Dt} = \frac{\gamma_1}{v_t}\tau_{ij}\frac{\partial u_i}{\partial x_j} - \beta_1\rho\omega^2 + \frac{\partial}{\partial x_j}\left[(\mu + \sigma_{\omega_1}\mu_t)\frac{\partial \omega}{\partial x_j}\right] \tag{9}$$

Transformed k - ϵ model: (Menter, 1994; Roy & Ducoin, 2016; Basumatary et al., 2018)

$$\frac{D\rho k}{Dt} = \tau_{ij}\frac{\partial u_i}{\partial x_j} - \beta^*\rho\omega k + \frac{\partial}{\partial x_j}\left[(\mu + \sigma_{k_2}\mu_t)\frac{\partial k}{\partial x_j}\right] \tag{10}$$

$$\frac{D\rho\omega}{Dt} = \frac{\gamma_2}{v_t}\tau_{ij}\frac{\partial u_i}{\partial x_j} - \beta_2\rho\omega^2 + \frac{\partial}{\partial x_j}\left[(\mu + \sigma_{\omega_2}\mu_t)\frac{\partial \omega}{\partial x_j}\right] + 2\rho\sigma\omega_2\frac{1}{\omega}\frac{\partial k}{\partial x_j}\frac{\partial \omega}{\partial x_j} \tag{11}$$

Original k - ω equations (8, 9) are multiplied by F_1 and transformed k - ϵ equations (10, 11) are multiplied by $(1 - F_1)$. The corresponding equations of each set are added together to give the SST k - ω model: (Menter, 1994; Roy & Ducoin, 2016)

$$\frac{D\rho k}{Dt} = \tau_{ij}\frac{\partial u_i}{\partial x_j} - \beta^*\rho\omega k + \frac{\partial}{\partial x_j}\left[(\mu + \sigma_{k_1}\mu_t)\frac{\partial k}{\partial x_j}\right] \tag{12}$$

$$\frac{D\rho\omega}{Dt} = \frac{\gamma}{v_t}\tau_{ij}\frac{\partial u_i}{\partial x_j} - \beta\rho\omega^2 + \frac{\partial}{\partial x_j}\left[(\mu + \sigma_\omega\mu_t)\frac{\partial \omega}{\partial x_j}\right] + 2\rho(1 - F_1)\sigma\omega_2\frac{1}{\omega}\frac{\partial k}{\partial x_j}\frac{\partial \omega}{\partial x_j} \tag{13}$$

Let ϕ_1 represent any constant in the original model original k - ω equations, ϕ_2 any constant in the transformed k - ϵ. So, the ϕ corresponding constant of the SST k - ω model, are related as follows:

$$\phi = \phi_1 F_1 + \phi_2(1 - F_1) \tag{14}$$

Here the value of the function F_1 is designed to be one in the near wall area (to activate the original model) and zero when away from the surface. This blending occurs in the wake region of the boundary layer. Where

$$F_1 = \tanh(arg_1^4) \tag{15}$$

$$arg_1 = \min\left(\max\left(\frac{\sqrt{k}}{0.09\omega y}; \frac{500v}{y^2\omega}\right); \frac{4\rho\sigma\omega_2 k}{CD_{k\omega}y^2}\right. \tag{16}$$

$$CD_{k\omega} = \max\left(2\rho\sigma\omega_2\frac{1}{\omega}\right)\frac{\partial k}{\partial x_j}\frac{\partial \omega}{\partial x_j}, 10^{-20} \tag{17}$$

and the turbulent kinetic viscosity (v_t) as:

$$v_t = \frac{a_1 k}{\max(a_1\omega; \Omega F_2)} \tag{18}$$

Where, arg_1 and arg_2 are the functions defined by Eqs. 16 and 20. The $CD_{k\omega}$ is the function related to the cross-diffusion term of Eq. 17. The F_1 and F_2 are the blending functions

$$F_2 = \tanh(arg_2^2) \tag{19}$$

$$arg_2 = \max\left(2\frac{\sqrt{k}}{0.09\omega y}; \frac{500v}{y^2\omega}\right) \tag{20}$$

The set of constants which are used for the original k - ω and k - ϵ model are as follows

Set (ϕ_1) (Wilcox k - ω model): (Menter, 1994; Roy & Ducoin, 2016)

$$\gamma_1 = \frac{\beta_1}{\beta^*} - \frac{\sigma_{\omega_1}k^2}{\sqrt{\beta^*}}$$

β^* = 0.09, k = 0.41, β_1 = 0.0750, $\sigma_{\omega 1}$ = 0.5, σ_{k1} = 0.5

Set (ϕ_2) (Transformed k - ϵ model): (Menter, 1994; Roy & Ducoin, 2016)

$$\gamma_2 = \frac{\beta_2}{\beta^*} - \frac{\sigma_{\omega_1}k^2}{\sqrt{\beta^*}}$$

β^* = 0.09, k = 0.41, β_2 = 0.0828, $\sigma_{\omega 2}$ = 0.856, σ_{k2} = 1.0

2.4 Numerical Schemes and Boundary Conditions

The numerical investigations are performed using the SST k - ω model, where the finite volume approach is utilized to discretize governing equations (Patankar, 1980). The second-order central difference scheme has been utilized to discretize the advective terms, whereas the second-order upwind scheme has been employed to

discretize the diffusive terms. The backward second-order implicit scheme has been implemented to discretize the transient terms. The velocity and the pressure in the governing equations are coupled using the PIMPLE scheme with two corrector loops. The symmetric Gauss-Seidel solver with an error tolerance of 10^{-6} is used to solve the momentum equations, and the pressure correction equation is solved using the GAMG (Geometrically Agglomerated Algebraic Multi-Grid Solver), which has a convergence criteria of 10^{-7} in each time step. A variable time step is considered to maintain the courant number less than or equal to 0.5 throughout the simulation. The time step for each iteration is approximately 1×10^{-4} seconds. The open-source CFD package, OpenFOAM (2017), has been used to achieve the numerical simulations.

The schematic diagram of present computational domain is illustrated in Fig. 2. At the inlet of the computational domain, a fully developed log velocity profile of magnitude U = 0.8 m/s has been considered. The turbulence intensity at the computational domain's inlet is assumed to be 2%, resulting in a more realistic flow. The viscosity of fluid is considered same as the viscosity of water (ν = 8.8 × 10^{-7} m^2/s) and the flow is considered incompressible which yields the Reynolds number Re = UD/ν = 2.25 × 10^5. The inlet is treated with zero pressure gradient boundary condition. The left and right walls of the water channel have been considered as the top and bottom boundaries of the computational domain. These walls are treated with no slip boundary condition where the pressure is treated as zero gradient. The outlet of the computational domain kept at zero-gauge pressure and the velocity is treated as zero gradient boundary condition. To ensure the connection and flow field consistency between the stationary and rotating domains, an Arbitrary Mesh Interface (AMI) zone is considered, which effectively takes the transient effects and shows rotating parts in a realistic way. In the present computation the AMI boundary surface is treated with cyclic boundary condition. The rotor blades are treated with no slip boundary condition and zero gradient boundary condition for velocity and pressure respectively. The rotating domain that includes the rotor blades is assigned angular motion (clockwise) depending on the tip speed ratio (TSR) used in various cases. The values of TSR varied from 0.5 to 1.3 at the interval of 0.1 for the each cases (*A*, *B* and *C*) considered in the present study. The boundary conditions that were applied at the computational domain boundaries are exhibited in Table 2.

Table 2 Boundary conditions

Inlet	U = 0.8 m/s, $\frac{\partial P}{\partial x} = \frac{\partial P}{\partial y} = 0$, $k = 1.5I^2$; $I = 2\%$, $\omega = \frac{k^{0.5}}{C_\mu^{0.25} L}$; $L = 0.07 * D$, $C_\mu = 0.09$
Outlet	$P = 0$, $\frac{\partial \xi}{\partial x} = \frac{\partial \xi}{\partial y} = 0$, where $\xi = U, k, \omega$
Left wall, right wall and rotor	$U = 0$, $\frac{\partial P}{\partial x} = \frac{\partial P}{\partial y} = 0$; k *and* ω are obtained from wall functions
AMI	$\zeta = cyclicAMI$, where $\zeta = U, P, k$ *and* ω

2.5 Domain Meshing and Grid Independence Test

The mesh in the computational domain of the present study has been generated using structured hexahedral cells, as shown in Fig. 3. The developed mesh has a total grid points of 147756 which creates 71786 cells and 289237 faces. Among the overall number of cells, 68856 are of hexahedral type, 2130 are of polyhedral type and 800 are of prisms type. In the transition zone of the mesh density, the polyhedral cells are appeared with various grid sizes as depicted in Fig. 3. The distribution of hexahedral (cubic) type cells is 95.92%, which reduces the time required for each iteration. Figure 4 illustrates a zoomed view of the present grid distribution near the rotor. The maximum and minimum sizes of the grid considered in the present mesh generation are 0.0384 m and 1.13 × 10^{-6} m, respectively, which is achieved by refining the mesh in six steps. Close to the boundary of the computational domain, the mesh is largest (Fig. 3), while the minimum grid size is present at the blade surface (Fig. 4b). The first grid point on the blade surface falls below in the laminar sublayer, with a value of $y^+ \cong 0.9$ close enough

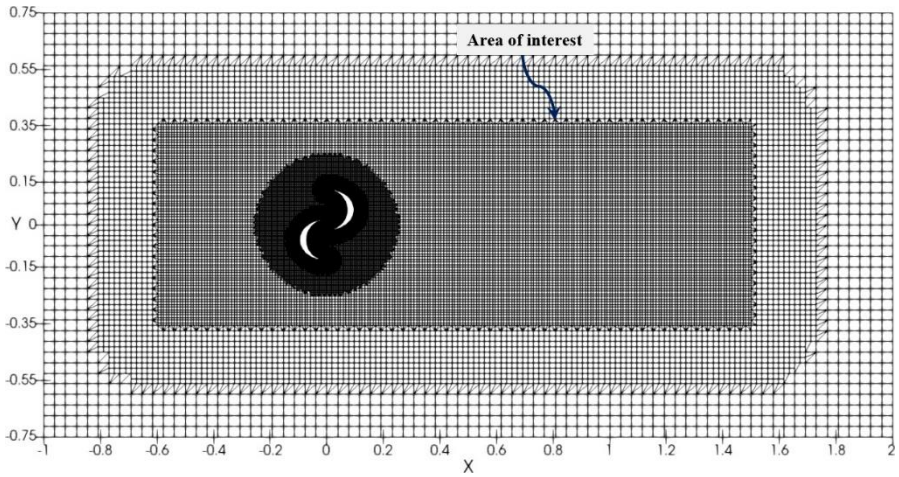

Fig. 3 Grid distribution in the computation domain

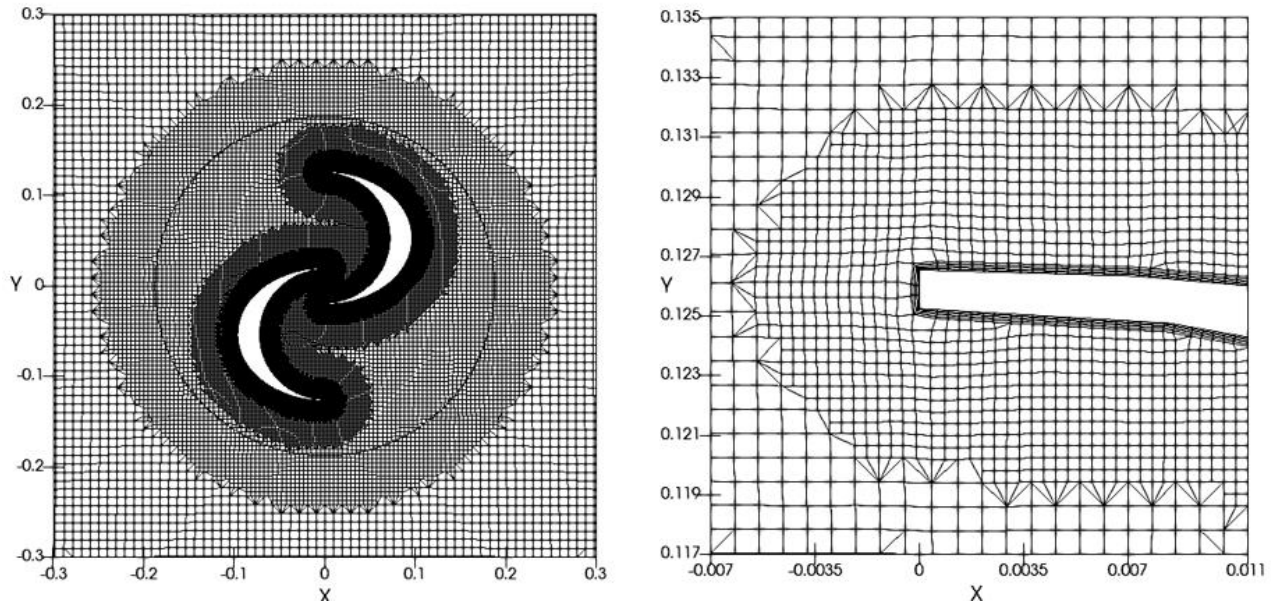

(a) Over the rotating domain. (b) Over the rotor blade.

Fig. 4 A zoomed view of the computational mesh close to the rotor

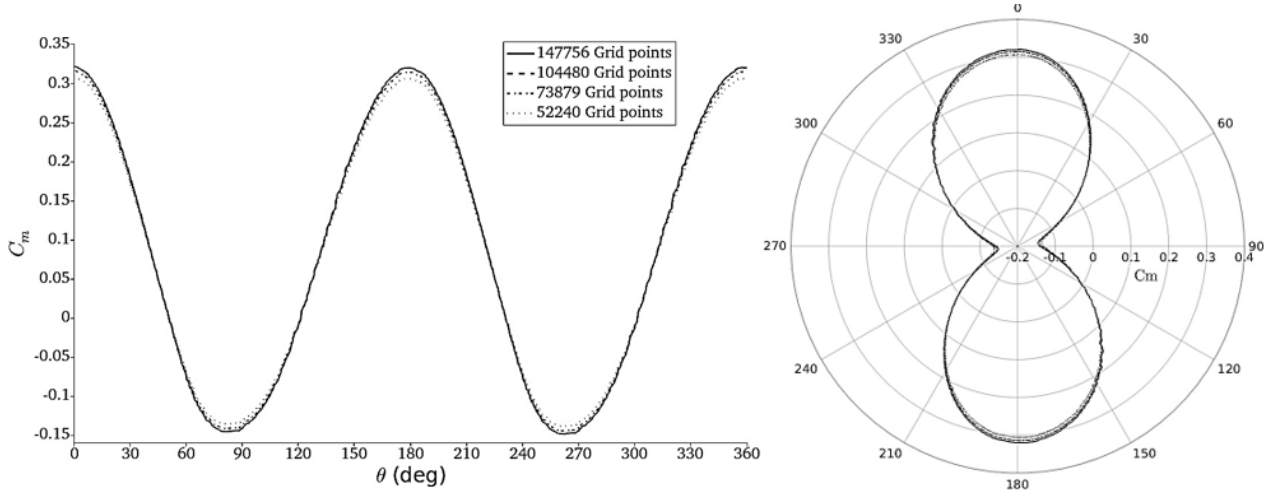

Fig. 5 Grid independence test

to capture the boundary layer phenomena. To capture the flow structure in the downstream, an "area of interest" has been created where adequate mesh refinement has been adopted, as shown in Fig. 3.

In the present analysis, all results are presented in the developed flow field, obtained by running the simulation for enough time (20 cycles) to remove initial transient flow from the computational domain. A grid independent test has been performed by collecting the torque coefficient (C_m) in one rotation of the rotor for different mesh sizes. The test is carried out primarily by changing the number of cells closer to the rotor and in the region of interest. Simultaneously, the case of the highest TSR = 1.3 has been considered for the test so that the same grid can be used for all other cases. Figure 5 shows the grid independence test results of four different grid resolutions. It is observed that the variation in coefficient of torque (C_m) for mesh with 147756 grid points closely matches that of the mesh with the 104480 grid points. A mesh with 147756 grid points has been considered for a reasonable numerical calculation in all other cases based on the grid independent test.

2.6 Numerical Validation

The numerical results obtained by Tian et al. (2017) using the SST k - ω turbulence model for the Savonius wind rotor are used to verify the accuracy of the present numerical simulation. They have presented the results of classical Savonius wind rotor working at the upstream velocity of 7 m/s. In the present work, the same configuration has been considered to verify the numerical procedure accuracy. Figure 6 shows the comparison of the variation of the torque coefficient (C_m) over one rotation of the rotor in the developed flow field with the results of Tian et al. (2017). Figure 6 indicates that the present result is in good agreement with the result of Tian et al. (2017). It confirms the accuracy of the numerical procedure

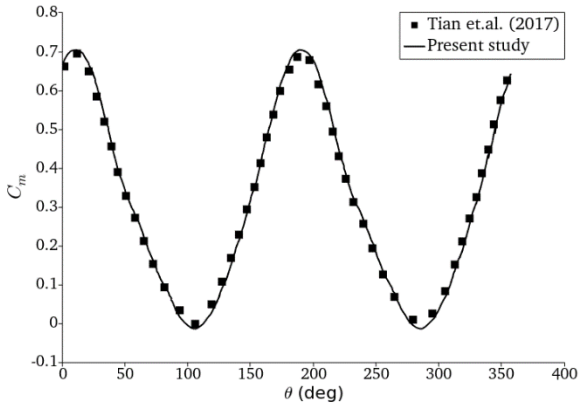

Fig. 6 Comparison of C_m with the results of Tian et al. (2017)

followed in the present work. Further, the shape of the rotor blades and the flow medium are modified with a semi-elliptical outer surface and water respectively. The various results obtained are discussed in the following sections.

3. RESULTS AND DISCUSSION

3.1 Coefficients of Power and Torque

In general, the performance of the rotor is described using the C_p and C_m. The variations in the coefficient of torque (C_m) with the rotor position have been compared for three cases, as illustrated in Fig. 7. The trend of variation in C_m, in all three cases is found to be almost similar. A significant change in the values of C_m is observed over the period of rotor position from 0˚ to 115˚. During this period of the rotor, mainly the outer surface of the returning blade and the inner surface of the advancing blade interact with upstream. Here it is realized that the significant improvement in the values of C_m is mainly due to the shape of the outer surface of the rotor as there is no difference in the shape of the inner surface for different cases. It confirms that the elliptical outer surface of the rotor has improved performance compared to the normal circular surface. This confirms that as the degree of ellipticity of the outer surface increases, it improves the rotor performance. The average C_p values are evaluated using Eq. 4, have been presented in Fig. 7. Where it is observed that the Case-*A* provides the maximum value of C_p compare to other cases.

The performance of the three rotors is analyzed by varying the TSR from 0.5 to 1.3 at an interval of 0.1, and the variations of averaged C_p and C_m as a function of TSR are depicted in Fig. 8. The C_p curves in the present study were compared with the experimental results of the conventional rotor (Hayashi et al., 2005; Patel et al., 2016; Nag & Sarkar, 2020), as depicted in Fig. 8a. It is observed that the trend of C_p for all three cases is similar to that of the experimental data provided (Hayashi et al., 2005; Patel et al., 2016; Nag & Sarkar, 2020). Here, the deviations in the results were observed due to the differences in the rotor's geometry and the flow medium. It is seen that the value of C_p increases with increase in TSR, attains a peak value, and then decreases as shown in Fig. 8a. Further increase in TSR will lead to a steady decrease in the values of C_p as expected by the literature (Basumatary et al., 2018; Talukdar et al., 2018; Salleh et al., 2019; Yao et al., 2019). In three cases, the highest value of C_p of 0.142 is obtained in Case-*A* which is 7.57% and 18.33% higher than Case-*B* and Case- *C* respectively. The peak C_p values obtained in the Case-*B* and Case-*C* rotors are 0.132 and 0.120. The power output of the rotor is calculated by considering that the height of the rotor is equal to its diameter. The maximum power output of the Case-*A* rotor is 2.32 W, whereas the power outputs of the Case-*B* and Case-*C* rotors are 2.16 W and 1.96 W, respectively. The C_m curves in the present study were compared with the experimental results of the conventional rotor (Kamoji et al., 2008; Golecha et al., 2011; Patel et al., 2016), as depicted in Fig. 8b. It is observed that the trend of C_m for all three cases is similar to that of the experimental data provided (Kamoji et al., 2008; Golecha et al., 2011; Patel et al., 2016). Here, the deviations in the results were observed due to the differences in the rotor's geometry and the flow medium. In Fig.e 8b, it is observed that the value of Case-*C* is found to be lower for each TSR value than in Case-*A* and Case-*B*. Simultaneously, there has been a steady decrease in the values of the average C_m in each case as the value of TSR increases.

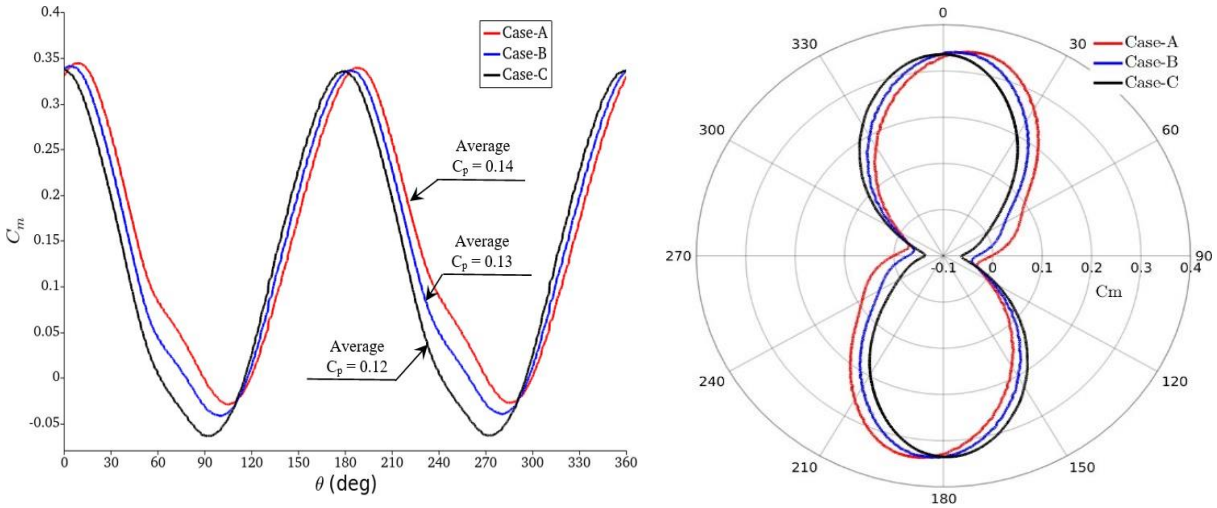

Fig. 7 Instantaneous C_m of the rotors at TSR 1.0

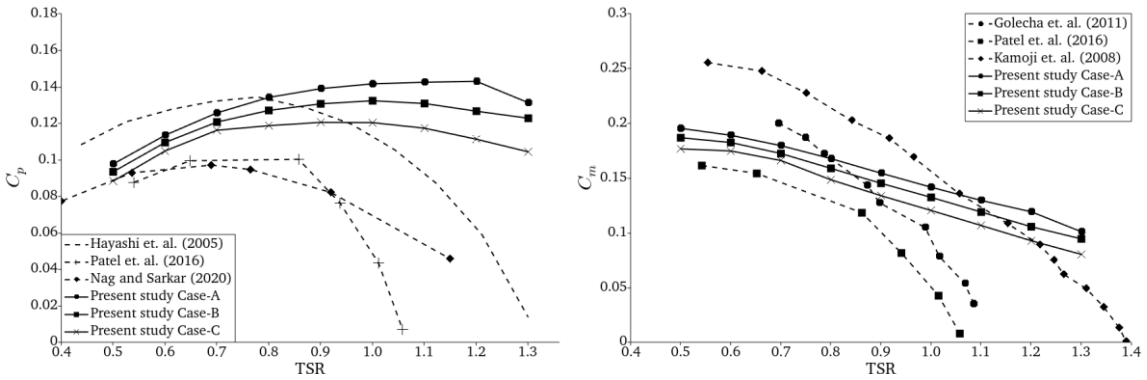

(a) Average C_p vs TSR (b)Average C_m vs TSR.

Fig. 8 Average C_p and C_m variations with respect to TSR for different cases

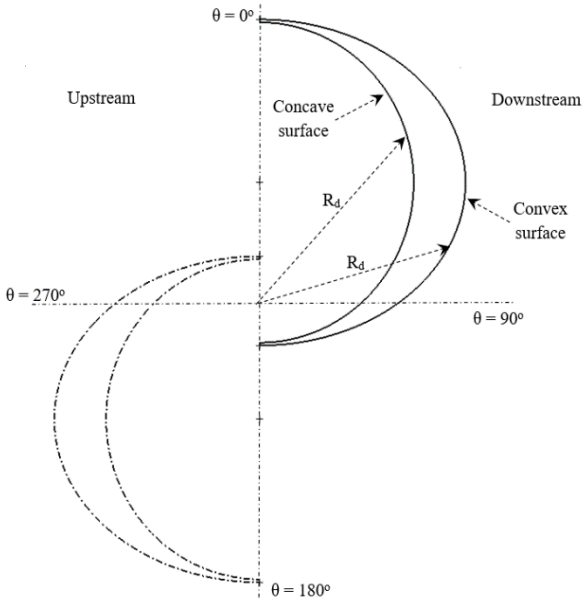

Fig. 9 Schematic diagram of a single rotor blade surfaces (Case-*A*) at $\theta = 0^{\circ}$

3.2 Pressure Distributions

The schematic diagram of the rotor blade (Case-*A*) at $\theta = 0^{\circ}$ is shown in Fig. 9. The rotor blade comprises two surfaces; the convex surface (blade outer surface) and the concave surface (blade inner surface). The location (R_d) over the blade surface (for both concave and convex), where the pressure values have been extracted, is measured from the rotor axis, as shown in Fig. 9. The comparison (among Case-*A*, Case-*B* and Case-*C*) of pressure distribution P/ρ m^2/s^2 on the surfaces of single rotor blades at different positions of the rotor is shown in Fig. 10. A complete one cycle of rotation is presented with an interval of 45°. Observation of the pressure distribution shows that there is a significant difference on the variation of pressure over the convex surface at each position of rotation. While comparatively less variation has been found over the concave surface.

At 0° (Fig. 10a), the pressure on the concave surface of Case-*A* is slightly higher than Case-*B* and Case-*C*. But, the convex surface of Case-*A* experiences less pressure compared to the other cases. The more pressure variation on the convex surface of the rotors are observed from R_d = 0.07 to 0.122. As the rotor reaches to 45° (Fig. 10b), the pressure on the concave surface of Case-*A* increases comparatively.

At this position of the rotor, a slight positive pressure has been noted between R_d = 0.11 to 0.124. Whereas the pressure on the convex surface attains higher positive values of pressure compared to the concave surfaces.

The surfaces of the rotor blade experiences the negative pressure as it reaches to 90° (Fig. 10c). The convex surface of the rotors experiencing the higher-pressure values than the concave surface as it is becoming a returning blade. The convex surface (Case-*A*) from R_d = 0.06 to 0.09 exhibits low pressure values, and from R_d = 0.09 to 0.12 exhibited the higher pressure comparatively. The values of pressure were found to be almost same over the concave surfaces at a rotor angle of 135° (Fig. 10d), which shows that the influence of fluid coming from the convex surface of the opposite blade is less. On the convex surfaces, the pressure reaches positive values from R_d = 0.05 to 0.11, whereas the surface (Case- *A*) in-between R_d = 0.05 to 0.075 shows a higher-pressure value comparatively. The Case-*A* shows the low-pressure values while the rotor moving from 135° to 225°, which reduces the opposing forces on the convex surface comparatively and improves the performance of the rotor. When the rotor reaches 270° (Fig. 10g), the overall pressure on the convex surface shifts to negative values. The convex surface (Case-*A*) shows higher pressure values among the other cases. At position 315° (Fig. 10h), the pressure values on the convex surfaces attains negative values. It is found in the study that with an increase in the radius of the semi-elliptical outer surface, the pressure values decrease between the rotor positions 0° − 225° (Fig. 10a-10f). Further, the rotor position 270° − 315°, shows that the pressure values of the semi-elliptical outer surface increases with its radius. It shows semi-elliptical outer surface improves the performance of the rotor on returning positions, whereas it deteriorates the performance in advancing blade position (270° − 315°). The concave surface is not modified in the present study, although it shows a slight variation of pressure over it. It is the influence of diverted fluid from the semi-elliptical outer surface of the opposite blade.

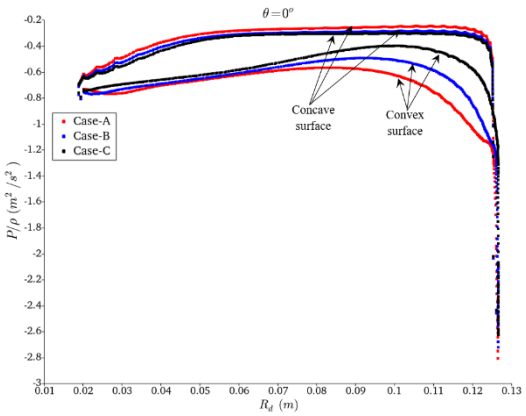

(a) At θ = 0^o.

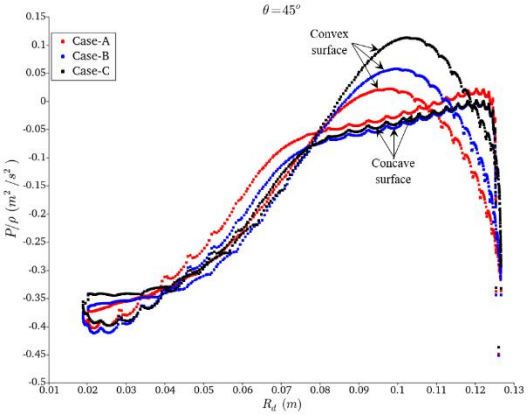

(b) At θ = 45^o.

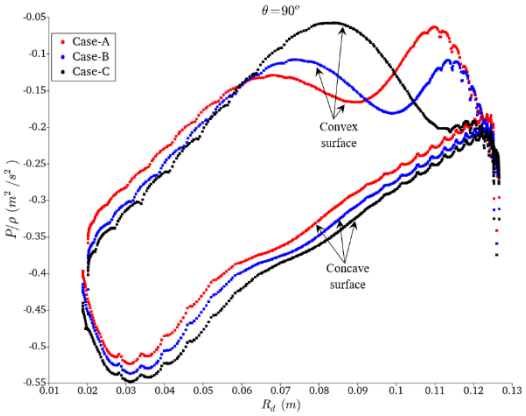

(c) At θ = 90^o.

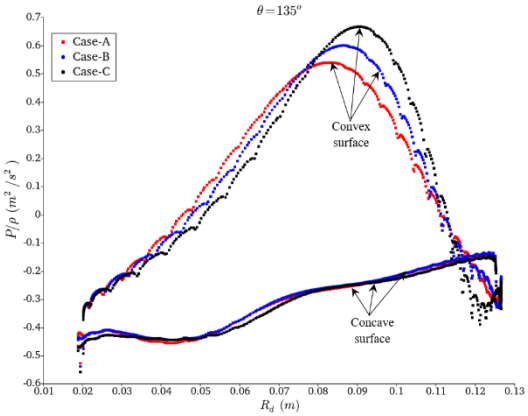

(d) At θ = 135^o.

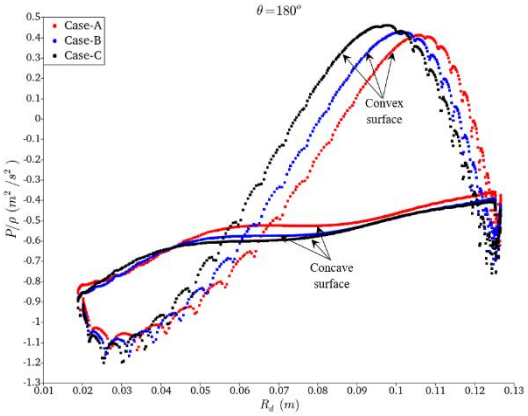

(e) At θ = 180^o.

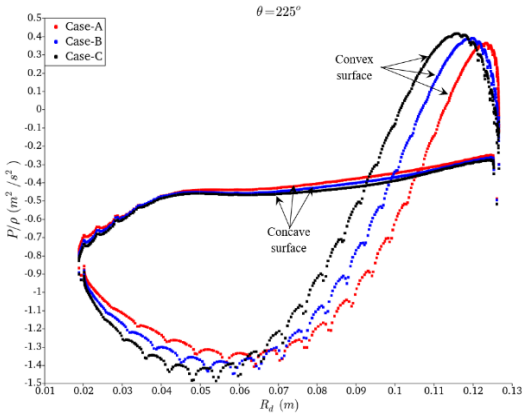

(f) At θ = 225^o.

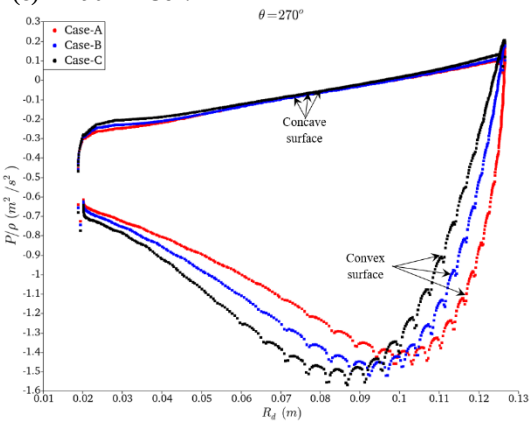

(g) At θ = 270^o.

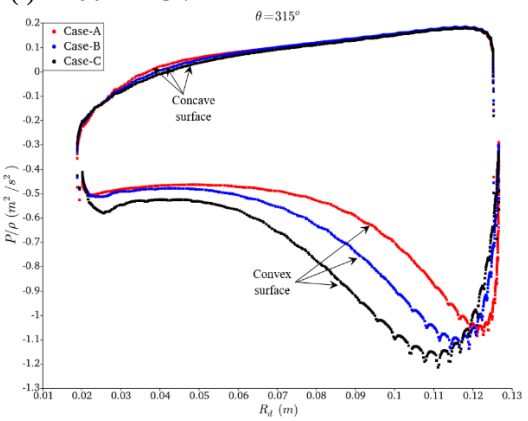

(h) At θ = 315^o.

Fig. 10 Comparison of pressure distribution on surfaces of rotor blades for cases *A*, *B* and *C* at TSR = 1.0 during one complete cycle of the rotor

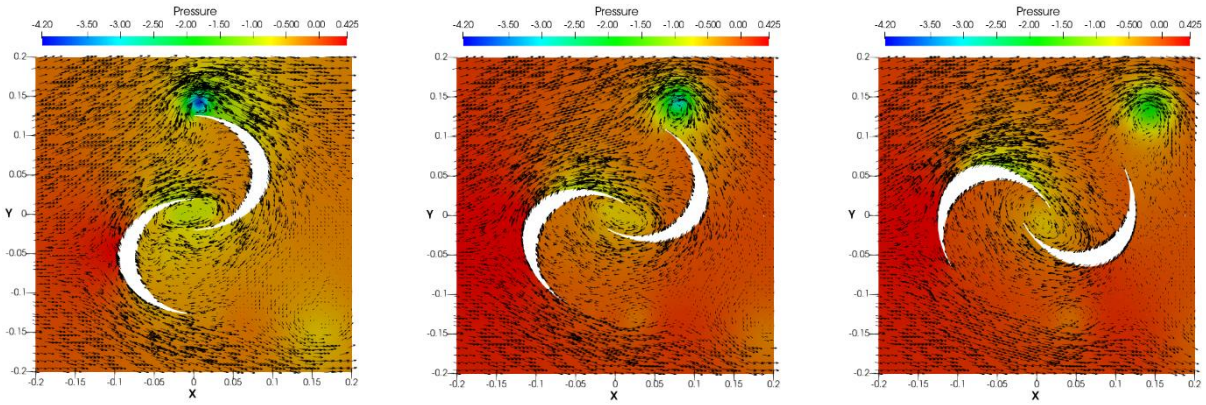

(a) $\theta = 0^o$ or 180^o. (b) $\theta = 30^o$. (c) $\theta = 60^o$.

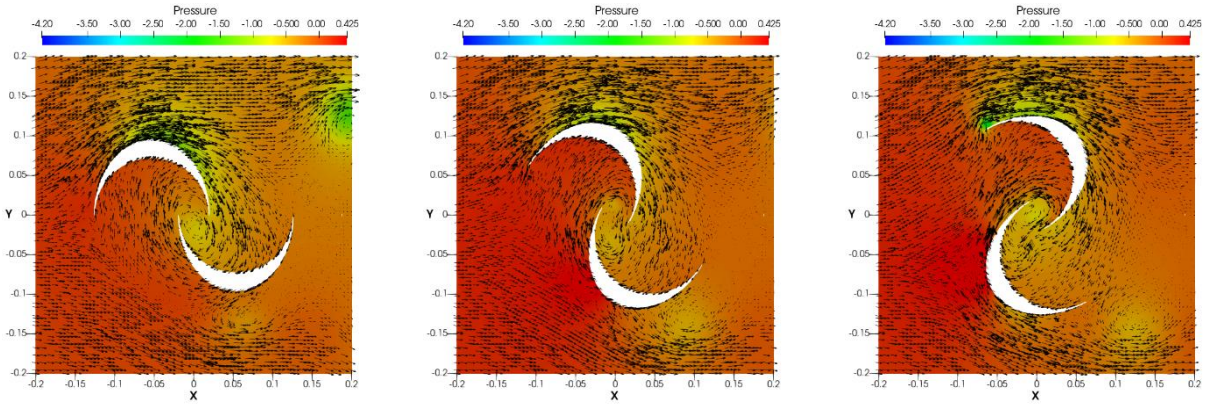

(d) $\theta = 90^o$. (e) $\theta = 120^o$. (f) $\theta = 150^o$.

Fig. 11 Velocity vectors over the contours of pressure at TSR= 1.0 for the Case-*A*

The Flow Characteristics

The flow pattern close to the rotor is presented on the contour plot of the pressure, using the velocity vector and streamline, as shown in Figs. 11 and 12, respectively. The flow field is presented at 30˚ intervals from 0˚ to 180˚ for the six stages of the rotor, covering half a cycle of rotation, since the next half cycle mimics the rotor's half cycle of rotation. The blade whose concave surface faces upstream is known as the advancing blade, whereas the blade whose convex surface faces upstream is known as the returning blade. In the rotor's initial position (0˚ or 180˚), when the advancing blades face upstream from its concave surface (Figs. 11a and 12a), which is capable of collecting most of the kinetic energy of the incoming fluid, a high value of torque (clockwise) is generated. Simultaneously, the returning blade's convex surface faces upstream, which diverts the fluid to either side and creates a stagnation zone, experiencing less torque (anticlockwise). Finally, the resulting torque produces a clockwise rotation of the rotor. When the rotor rotates, the returning blade diverts more fluid towards the advancing blade, as observed in the Figs. 11b, 11c, 12b and 12c, which helps to produce additional torque by the advancing blade.

This prompted the researcher to design an exquisitely convex surface for the returning blade. At the same time, a returning flow is created due to the rotor motion, which helps to move the returning blade in a clockwise direction, ultimately decreasing the negative torque that the returning blade generates. The fluid emerging from the concave surface of the advancing blade interacts with the mainstream and produces a tip vortex, as observed in Figs. 11a and 12a. At the same instant, another tip vortex is produced closer to the tip of the returning blade by the interaction between the diverted fluid from the returning flow and the returning blade. Interestingly, the tip vortex, which is formed near the advancing blade, immediately leaves the blade and becomes involved in the mainstream. Furthermore, the other tip vortex, created near the returning blade, is interacted with by the advancing blade, is strengthened, and then is left for the mainstream (as shown in Figs. 12d, 12e, and 12f). The vortex between the rotor blades, which has been observed in all stages of rotation (as shown in Fig. 12), is a result of the absence of a rotor axle in the current design. This particular design of rotor blades without an axle allows the flow to be bypassed by another blade, which helps in reducing vacuum formation behind the returning blades.

3.4 Shearing and Swirling Zones

The vortex distribution or blade–wake interaction in the flow field is usually analyzed using vortex contours. However, these contours of the vortex component $\left(\omega_z = \frac{1}{2}\left(\frac{\partial u}{\partial y} - \frac{\partial v}{\partial x}\right)\right)$ are not fully capable of distinguishing between shearing and swirling zones in the flow field (Jeong & Hussain, 1995). To show these

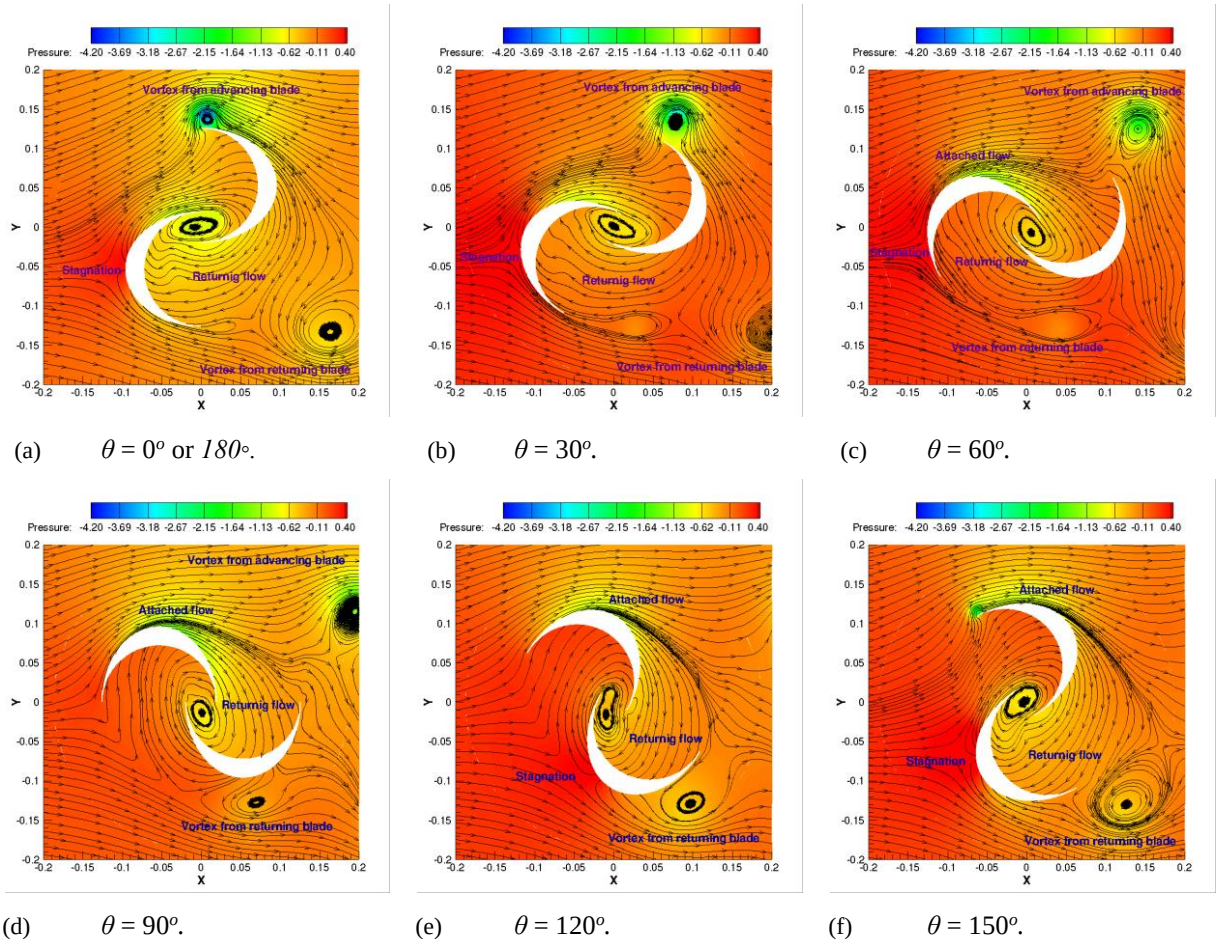

(a) $\theta = 0^o$ or 180^o. (b) $\theta = 30^o$. (c) $\theta = 60^o$.

(d) $\theta = 90^o$. (e) $\theta = 120^o$. (f) $\theta = 150^o$.

Fig. 12 Streamlines over the contours of pressure at TSR= 1.0 for the Case-*A*

shearing and swirling regions Jeong & Hussain (1995) proposed the λ_2 criterion as follows

$$\lambda_2 = \left(\frac{\partial U}{\partial x} + \frac{\partial v}{\partial y}\right)^2 - 4\left(\frac{\partial u}{\partial x}\frac{\partial v}{\partial y} - \frac{\partial u}{\partial y}\frac{\partial v}{\partial x}\right) \qquad (21)$$

In this λ_2 criterion, the negative and positive values of λ_2 represent the pure swirling and shearing regions in the flow field. Whereas the negative and positive values of ω_z are capable to show the direction of rotation in counterclockwise and clockwise. In the following discussion, the existence vortex and direction of rotation have been identified using the contours of λ_2 and ω_z. The evolution in wake structures around the rotor (case-*C*) at various angular positions are analyzed using the contours of λ_2 and ω_z in Fig. 13.

Since the rotor's half cycle of rotation mimics the next half cycle, the flow field is presented at 45˚ intervals from 0˚ to 180˚ for the four stages of the rotor, covering half a cycle of rotation. It is observed that the tip vortex of the advancing blade develops somewhere at the blade angle θ = 135˚ (Fig. 13d), which leaves the blade around θ = 45˚ (Fig. 13b) while continuously developing in size. These vortices rotate in clockwise direction, as seen from Figs 13h, 13e and 13f. As the blade approaches angle θ = 0˚ (Fig. 13a), the tip vortex of the returning blade is developed, which leaves the blade around θ = 90˚ (Fig. 13c) while continuously developing in size. These vortices rotate in counter- clockwise direction, as seen from Figs 13e, 13f and 13g. A clockwise motion vortex is found in all positions of the overlap region of the rotor blades. Although vortex in the overlap region is found to be more affected by the diverted flow of the advancing blade (Fig. 13a and 13d). Figure 13a, 13b and 13d shows a formation of vortices behind the advancing blade represents the small structure of fluid spin (clockwise) over the surface of advancing blade. The advantages of the λ_2 plot over the ω_z plot can be observed in Figs 13c and 13g. The λ_2 plot (Fig. 13c) clearly shows the detachment of tip vortices from the returning blade, whereas the ω_z plot (Fig. 13g) is unable to predict the detachment of tip vortices from the returning blade correctly.

3.5 Turbulent Kinetic Energy

Figure 14 shows the instantaneous turbulent kinetic energy $\left(k = \frac{1}{2}\left(\overline{(u')^2} + \overline{(v')^2} + \overline{(w')^2}\right)\right)$ distribution of the rotor (Case-*C*) at different angular positions. Since the rotor's half cycle of rotation mimics the next half cycle, the flow field is presented at 45˚ intervals from 0˚ to 180˚ for the four stages of the rotor, covering half a cycle of rotation. The values of *k* are developing in the flow field due to the interaction between the rotor blades and fluid. The high values of *k* are observed to develop near the

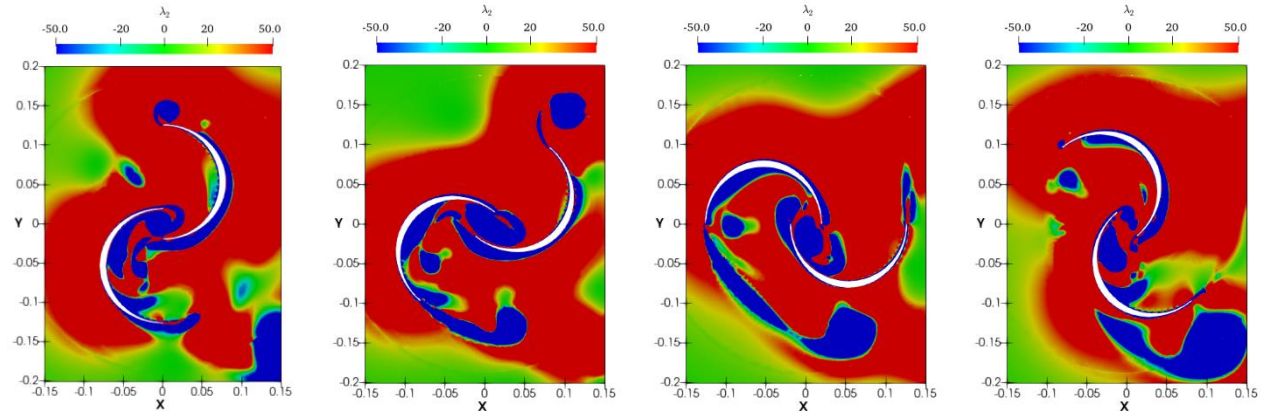

(a) λ_2 *at* $\theta = 0^o$ or *180*◦. (b) λ_2 *at* $\theta = 45^o$. (c) λ_2 *at* $\theta = 90^o$. (d) λ_2 *at* $\theta = 135^o$.

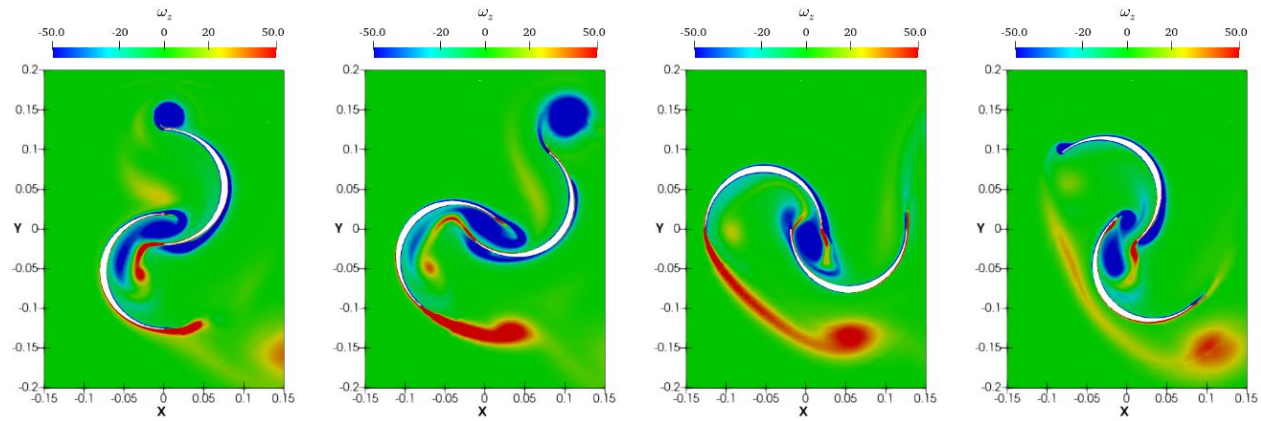

(e) ω_z *at* $\theta = 0^o$ or *180*◦. (f) ω_z *at* $\theta = 45^o$. (g) ω_z *at* $\theta = 90^o$. (h) ω_z *at* $\theta = 135^o$.

Fig. 13 Contours of λ_2 and ω_z for one rotation of rotor (case-*C*) at TSR = 1.0

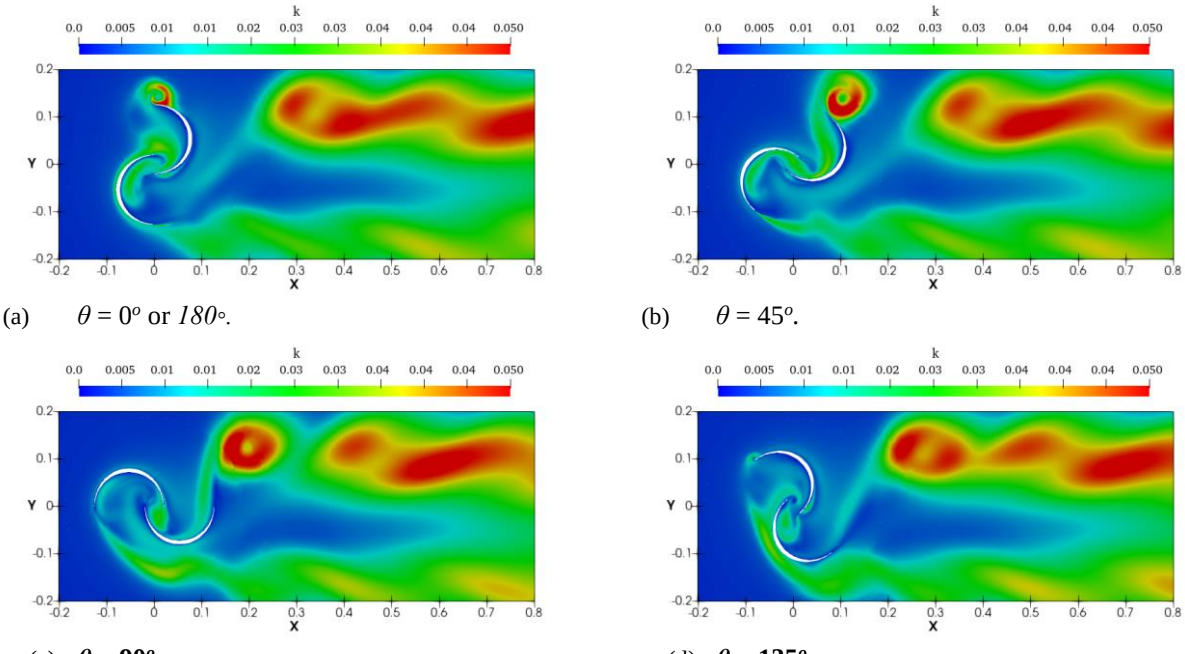

(a) $\theta = 0^o$ or *180*◦. (b) $\theta = 45^o$.

(c) $\theta = 90^o$. (d) $\theta = 135^o$.

Fig. 14 Contour of *k* for one rotation of the rotor (case-*C*) at TSR = 1.0

advancing blade at blade angle θ = 135° (Fig. 14d). Mixing with the eddies formed near the advancing blade tip at an angle θ = 0° (Fig. 14a), results in extremely high values of *k* and these high values of *k* are observed leaving the advancing blade tip at θ = 45° (Fig. 14b). It is observed that the values of *k* generated near the overlap region and returning blade tip at all positions of the rotor are lower compared to the values of *k* near the advancing blade tip. It can be observed that the low values of *k* that were developed near the outer surface of the returning blade (as depicted in Fig. 14d) are moved towards the tip of the returning blade by the effect of the elliptic outer surface of

the blade. In all the positions of the rotor (Figures 14a, 14b, 14c and 14d), high and low values of k are originating from the advancing blade tip and returning blade tip were observed moving downstream with shear between them and maintaining turbulent kinetic energy across the flow.

4. CONCLUSION

The present 2D numerical analysis has been performed to improve the coefficient of power (C_p) of the Savonius Hydrokinetic Turbine (SHT) by altering the outer surface of the rotor blades. Three different cases (Case-*A*, Case-*B* and Case-*C*) of rotor blades were achieved by changing the principal radius (r_A, r_B and r_C) of the semi-elliptical outer surface to reduce opposing forces on the returning blades. The radius (r) of the inner circular surface of the rotor is kept constant. These cases were investigated by varying the values of TSR from 0.5 to 1.3 while maintaining a constant channel inflow velocity of 0.8 m/s. The turbulent incompressible flow field has been solved using the SST k - ω model, and conclusions were drawn based on the qualitative and quantitative results obtained.

- The developed semi-elliptical outer surface gives the rotor an aerodynamic shape that minimizes the effect of drag forces on the blades while returning, as well as helps to direct the flow towards the advancing blades at high speeds. As a result, an additional power output has been observed.
- The developed semi-elliptical outer surface in- creases the instantaneous values of C_m between rotation angles of 0° and 115°. During which the returning blades primarily interact with the in- coming flow.
- The power output of the rotor is calculated by considering that the height of rotor is equal to its diameter. The maximum power output of the Case-*A* rotor is 2.32 W, whereas the power outputs of the Case-*B* and Case-*C* rotors are 2.16 W and 1.96 W, respectively.
- The highest value of C_p of 0.142 is obtained in Case-*A* which is 7.57% and 18.33% higher than Case-*B* and Case-*C* respectively.
- A precise identification of the shearing and swirling zone is presented using λ_2 criterion since the ω_z contours only shows the direction of rotation.
- It is found in the study that with increase in the radius of semi-elliptical outer surface the pressure values decreases between the rotor positions $0^\circ - 225^\circ$. Further the rotor position $270^\circ - 315^\circ$, shows the pressure values of the semi-elliptical outer surface increases with its radius.

In the present analysis, various cases has been tested at a particular channel velocity (Re = 2.25×10^5). The study can be extended to investigate rotor performance at different channel velocities. Further improvement in rotor performance can be studied by adding airfoil blades, guided vanes and deflector plates on the upstream side of the flow field.

CONFLICT OF INTEREST

The authors declare that they have no conflict of interest.

AUTHORS CONTRIBUTION

Gudlavalleti Vamsi Babu: Conceptualization, Investigation, Methodology, Software, Validation, Writing - original draft, Writing - review & editing.

Devendra Kumar Patel: Conceptualization, Methodology, Software, Validation, Writing - review & editing.

REFERENCES

Abdelghafar, I., Kerikous, E., Hoerner, S., & Thévenin, D. (2023). Evolutionary optimization of a Savonius rotor with sandeel-inspired blades. Ocean Engineering, 279. https://doi.org/10.1016/j.oceaneng.2023.114504

Alizadeh, H., Jahangir, M. H., & Ghasempour, R. (2020). CFD-based improvement of Savonius type hydrokinetic turbine using optimized barrier at the low-speed flows. *Ocean Engineering*, *202*, 107178. https://doi.org/10.1016/j.oceaneng.2020.107178

Al-Obaidi, A. (2023a). Effect of different guide vane configurations on flow field investigation and performances of an axial pump based on CFD analysis and vibration investigation. *Experimental Techniques.* https://doi.org/10.1007/s40799-023-00641-5

Al-Obaidi, A. R. & Alhamid, J. (2023). Investigation of the main flow characteristics mechanism and flow dynamics within an axial flow pump based on different transient load conditions. *Iranian Journal of Science and Technology Transactions of Mechanical Engineering*, 47, 1397–1415.https://doi.org/10.1007/s40997-022-00586-x

Al-Obaidi, A. (2018). *Experimental and numerical investigations on the cavitation phenomenon in a centrifugal pump.* [Doctoral thesis, University of Huddersfield]. http://eprints.hud.ac.uk/id/eprint/34513/

Al-Obaidi, A. R. (2019). Investigation of effect of pump rotational speed on performance and detection of cavitation within a centrifugal pump using vibration analysis. *Heliyon, 5*. https://doi.org/10.1016/j.heliyon.2019.e01910

Al-Obaidi, A. R. (2023b). Experimental diagnostic of cavitation flow in the centrifugal pump under various impeller speeds based on acoustic analysis method. *Archives of Acoustics*, *48*(2), 159–170. https://doi.org/10.24425/aoa.2023.145234

Al-Obaidi, A. R., Khalaf, H. A. & Alhamid, J. (2023a). *Investigation of the influence of varying operation configurations on flow behaviors characteristics and hydraulic axial-flow pump performance*. ICONSEIR. http://dx.doi.org/10.4108/eai.24-11-2022.2332719

Al-Obaidi, A. R., Khalaf, H. A. & Alhamid, J. (2023b). *Investigation on the characteristics of internal flow within three-dimensional axial pump based on different flow conditions.* ICONSEIR. http://dx.doi.org/10.4108/eai.24-11-2022.2332720

Al-Obaidi, A., & Qubian, A. (2022). Effect of outlet impeller diameter on performance prediction of centrifugal pump under single-phase and cavitation flow conditions. *International Journal of Nonlinear Sciences and Numerical Simulation*, *23*(7-8), 1203-1229. https://doi.org/10.1515/ijnsns-2020-0119

Anthony, A. Z. & Roy, S. (2020). *Performance analysis of a modified Savonius hydrokinetic turbine blade for rural application.* IOP Conference Series: Materials Science and Engineering, 943. https://doi.org/10.1088/1757-899X/943/1/012034

Salleh, M. B., Kamaruddin, N. M., & Mohamed-Kassim, Z. (2019). Savonius hydrokinetic turbines for a sustainable river-based energy extraction: A review of the technology and potential applications in Malaysia. *Sustainable Energy Technologies and Assessments*, *36*, 100554. https://doi.org/10.1016/j.seta.2019.100554

Basumatary, M., & Biswas, A. (2016). Numerical simulation of two-bladed Savonius water turbine with deflector. *International Journal of Renewable Energy Technology*, *7*(4), 383. https://doi.org/10.1504/IJRET.2016.080115

Basumatary, M., Biswas, A., & Misra, R. D. (2018). CFD analysis of an innovative combined lift and drag (CLD) based modified Savonius water turbine. *Energy Conversion and Management*, *174*, 72–87. https://doi.org/10.1016/j.enconman.2018.08.025

Boccaletti, C., Fabbri, G., Marco, J., & Santini, E. (2008). An overview on renewable energy tech- nologies for developing countries: The case of Guinea Bissau. *Renewable Energy and Power Quality Journal*, *1*(6), 343–348. https://doi.org/10.24084/repqj06.295

Chen, Y., Chen, Y., Zhou, J., Guo, P., & Li, J. (2023). Optimization and performance study of bidirectional Savonius tidal turbine cluster with deflectors. *Energy Conversion and Management*, *283*. https://doi.org/10.1016/j.enconman.2023.116947

Golecha, K., Eldho, T. I., & Prabhu, S. V. (2011). Influence of the deflector plate on the performance of modified Savonius water turbine. *Applied Energy*, *88*, 3207–17. https://doi.org/10.1016/j.apenergy.2011.03.025.

Hayashi, T., Li, Y., & Hara, Y. (2005). Wind tunnel tests on a different phase three-stage Savonius rotor. *JSME International Journal, Series B: Fluids and Thermal Engineering*, *48*(1), 9–16. https://doi.org/10.1299/jsmeb.48.9

Jeong, J., & Hussain, F. (1995). On the identification of a vortex. *Journal of Fluid Mechanics*, *285*, 69–94. https://doi.org/10.1017/S0022112095000462

Kacprzak, K., Liskiewicz, G., & Sobczak, K. (2013). Numerical investigation of conventional and modified Savonius wind turbines. *Renewable Energy*, *60*, 578–585. http://dx.doi.org/10.1016/j.renene.2013.06.009

Kailash, G., Eldho, T. I., & Prabhu, S. V. (2012). Performance study of modified savonius water turbine with two deflector plates. *International Journal of Rotating Machinery*, *2012*. https://doi.org/10.1155/2012/679247

Kamal, M. M., & Saini, R. P. (2022). A review on modifications and performance assessment techniques in cross-flow hydrokinetic system. *Sustainable Energy Technologies and Assessments*, *51*, 101933. https://doi.org/10.1016/j.seta.2021.101933

Kamoji, M. A., Kedare, S. B., & Prabhu, S. V. (2008). Experimental investigations on single stage, two stage and three stage conventional Savonius rotor. *International Journal of Energy Research*, *32*, 877–895. https://doi.org/10.1002/er.1399

Khan, M. N. I., Tariq Iqbal, M., Hinchey, M., & Masek, V. (2009). Performance of savonius rotor as a water current turbine. *Journal of Ocean Technology*, *4*(2), 71–83. http://research.library.mun.ca/id/eprint/235

Kumar, A., & Saini, R. P. (2017). Performance analysis of a single stage modified Savonius hydrokinetic turbine having twisted blades. *Renewable Energy*, *113*, 461–478. https://doi.org/10.1016/j.renene.2017.06.020

Mahmoud, N. H., El-Haroun, A. A., Wahba, E., & Nasef, M. H. (2012). An experimental study on improvement of Savonius rotor performance. *Alexandria Engineering Journal*, *51*(1), 19–25. http://dx.doi.org/10.1016/j.aej.2012.07.003

Menter, F. R. (1994). Two-equation eddy-viscosity turbulence models for engineering applications. *AIAA Journal*, *32*(8), 1598–1605. https://doi.org/10.2514/3.12149

Mohamed, M. H., Janiga, G., Pap, E., & Thévenin, D. (2010). *Optimal performance of a modified three-blade savonius turbine using frontal guiding plates.* Proceedings of the ASME Turbo Expo. https://doi.org/10.1115/GT2010-22538

Nag, A. K. & Sarkar, S. (2020). Experimental and numerical study on the performance and flow pattern of different Savonius hydrokinetic turbines with varying duct angle. *Journal of Ocean Engineering and Marine Energy*, 6, 31–53. https://doi.org/10.1007/s40722-019-00155-6

OpenFOAM (2017). *The Open Source CFD Toolbox User Guide*.https://www.openfoam.com/documentation/user-guide.

Patankar, S. (1980). *Numerical heat transfer and fluid flow*. CRC press.

Patel, V., Bhat, G., Eldho, T. I., & Prabhu, S. V. (2016). Influence of overlap ratio and aspect ratio on the performance of Savonius hydrokinetic turbine. *International Journal of Energy Research*, *41*(6),

829– 844. https://doi.org/10.1002/er.3670

Roy, S., & Ducoin, A. (2016). Unsteady analysis on the instantaneous forces and moment arms acting on a novel Savonius-style wind turbine. *Energy Conversion and Management*, *121*, 281–296. http://dx.doi.org/10.1016/j.enconman.2016.05.044

Salleh, M. B., Kamaruddin, N. M., & Mohamed Kassim, Z. (2020). The effects of a deflector on the self-starting speed and power performance of 2- bladed and 3-bladed Savonius rotors for hydrokinetic application. *Energy for Sustainable Development*, *61*(1), 168–180. https://doi.org/10.1016/j.esd.2021.02.005

Sarma, N. K., Biswas, A., & Misra, R. D. (2014). Experimental and computational evaluation of Savonius hydrokinetic turbine for low velocity condition with comparison to Savonius wind turbine at the same input power. *Energy Conversion and Management*, *83*, 88–98. https://doi.org/10.1016/j.enconman.2014.03.070

Setiawan, P. A., Yuwono, T., & Widodo, W. A. (2019a). Effect of a circular cylinder in front of advancing blade on the savonius water turbine by using transient simulation. *International Journal of Mechanical and Mechatronics Engineering*, *19*(1), 151–159. https://api.semanticscholar.org/CorpusID:221793287

Setiawan, P. A., Yuwono, T., Widodo, W. A., Julianto, E., & Santoso, M. (2019b). Numerical study of a circular cylinder effect on the vertical axis savonius water turbine performance at the side of the advancing blade with horizontal distance variations. *International Journal of Renewable Energy Research*, *9*(2), 978–985. https://doi.org/10.20508/ijrer.v9i2.8890.g7662

Talukdar, P. K., Sardar, A., Kulkarni, V., & Saha, U. K. (2018). Parametric analysis of model Savonius hydrokinetic turbines through experimental and computational investigations. *Energy Conversion and Management*, *158*, 36–49. https://doi.org/10.1016/j.enconman.2017.12.011

Tartuferi, M., D'Alessandro, V., Montelpare, S., & Ricci, R. (2015). Enhancement of savonius wind rotor aerodynamic performance: A computational study of new blade shapes and curtain systems. *Energy*, *79*(C), 371–384. http://dx.doi.org/10.1016/j.energy.2014.11.023

Tian, W., Mao, Z., Zhang, B., & Li, Y. (2017). Shape optimization of a Savonius wind rotor with different convex and concave sides. *Renewable Energy*, *117*, 287–299. https://doi.org/10.1016/j.renene.2017.10.067

Tian, W., Song, B., Van Zwieten, J. H., & Pyakurel, P. (2015). Computational fluid dynamics prediction of a modified savonius wind turbine with novel blade shapes. *Energies*, *8*(8), 7915–7929. https://doi.org/10.3390/en8087915

Wahyudi, B., Soeparman, S., Wahyudi, S., & Denny, W. (2013). A Simulation study of flow and pres- sure distribution patterns in and around of tan- dem blade rotor of Savonius (TBS) hydrokinetic turbine model. *Journal of Clean Energy Technologies*, 286–291. https://doi.org/10.7763/jocet.2013.v1.65

Wong, K. H., Chong, W. T., Sukiman, N. L., Poh, S. C., Shiah, Y. C., & Wang, C. T. (2017). Performance enhancements on vertical axis wind turbines using flow augmentation systems: A review. *Renewable and Sustainable Energy Reviews*, *73*, 904–921. https://doi.org/10.1016/j.rser.2017.01.160

Yao, J., Li, F., Chen, J., Yuan, Z., & Mai, W. (2019). Parameter analysis of savonius hydraulic turbine considering the effect of reducing flow velocity. *Energies*, 13. https://doi.org/10.3390/en13010024

Zhao, Z., Zheng, Y., Xu, X., Liu, W., and Hu, G. (2009). Research on the improvement of the performance of savonius rotor based on numerical study. *1st International Conference on Sustainable Power Generation and Supply*, *SUPERGEN* 09, 1–6. https://doi.org/10.1109/SUPERGEN.2009.5348197